

Finite-Element Analysis of Valence Band Structure and Optical Properties of Quantum-Wire Arrays on Vicinal Substrates

Jong Chang Yi and Nadir Dagli, *Member, IEEE*

Abstract—The valence subband dispersion of quantum-wire arrays grown on vicinal substrates in GaAs–Al_xGa_{1-x}As material system is calculated using a finite-element method with periodic boundary conditions. The variational functional for the Luttinger–Kohn Hamiltonian is derived using the integration by parts with proper boundary conditions. The validity of this method is confirmed by calculating subband structure of quantum wells and rectangular quantum wires. Along with the electronic band structure, a detailed study of gain in the quantum-wire arrays with rectangular and serpentine shapes is presented, including the effect of coupling between wires and polarization dependence of the momentum matrix element. Finally, these results are compared to those of quantum wells.

I. INTRODUCTION

QUANTUM wires (QWR) which result due to quantum confinement in two dimensions have undergone extensive study and development for their interesting physical phenomena and potential device applications [1]–[3]. However, to observe significant quantum effects at room temperature, the carriers should spatially be confined in two dimensions to less than the exciton radius in an unconfined structure [3]. Recent developments in crystal growth techniques on vicinal and patterned substrates [4]–[6] have made it possible to fabricate quantum-wire arrays with very small lateral dimensions. Among these quantum-wire arrays, the tilted superlattice [4] (TSL), which has rectangular cross section, and the serpentine superlattice [6] (SSL), which has parabolic lateral interfaces, offer the possibility of sub-100 Å lateral dimensions.

The calculations of the energy band diagram and the wave function of structures with two-dimensional quantum confinement are generally very complicated. In general, they cannot be done analytically, except for special circumstances such as isotropic cylindrical quantum wires with infinite potential barrier height [7]. Recently, several numerical techniques have been developed for the analysis of quantum-wire structures, which include finite-element method [8], [9] (FEM), finite-difference method [10] (FDM), effective bond orbital method [11] (EBOM), and tight binding method [12] (TBM). Although EBOM and TBM can describe the electronic band structure

accurately, they require more than 18 basis functions at each atomic site, thus they require massive memory and processor time [11], [12]. However, FEM and FDM require only 4 or 6 basis function, respectively, depending on whether the spin-orbit split-off bands are neglected or not. The advantage of FEM as a numerical technique over FDM is that it can utilize a nonuniform mesh, hence the energy eigenstates and wavefunctions of arbitrarily shaped geometries with wide range of lateral dimensions can be analyzed accurately [8]. The disadvantage of the FEM compared to FDM, however, is that the formulation of the variational functional for the given multiband Hamiltonian is generally complicated. In this study, we first present a systematic implementation of the Luttinger–Kohn Hamiltonian [13] in the finite-element scheme for quantum-well and quantum-wire structures for arbitrary crystal orientation. The corresponding variational functional satisfying Euler equation [14] is derived for the first time by integration by parts with proper boundary conditions. Next, the accuracy of the method is verified by comparing its results to published results on quantum wells and wires. Then this finite-element method is applied to calculate the valence and conduction subband dispersion of tilted and serpentine superlattices which are GaAs quantum-wire arrays grown on vicinal substrates. The effects of wire-to-wire coupling on density of states and optical properties are quantitatively investigated. The polarization dependence of the optical transition involving heavy hole-like subbands and light hole-like subbands is graphically presented. The material gain and modal gain of TSL and SSL are also calculated and compared to a quantum-well structure.

II. METHOD OF ANALYSIS

If one neglects the effects of spin-orbit split-off bands on the valence band structure, one can use a four band $\mathbf{k}\cdot\mathbf{p}$ analysis for its investigation. Then the top of the valence band can be described as a solution of coupled equations given by

$$[\mathbf{H}_{LK} + (V(\mathbf{r}) - E)\mathbf{I}]\mathbf{J}_V = 0. \quad (1)$$

$V(\mathbf{r})$ is the confining potential, \mathbf{I} is the 4×4 unity matrix, and E is the energy eigenvalue. \mathbf{H}_{LK} is the Luttinger–Kohn Hamiltonian [13] which is

$$\mathbf{H}_{LK} = \begin{bmatrix} P & L & M & 0 \\ L^\dagger & Q & 0 & M \\ M^\dagger & 0 & Q & -L \\ 0 & M^\dagger & -L^\dagger & P \end{bmatrix} \quad (2)$$

Manuscript received July 27, 1993; revised June 15, 1994. This work was supported by Quest, the NSF Science and Technology Center for Quantized Electronic Structures, under Grant DMR 91-20007.

The authors are with the Department of Electrical and Computer Engineering, University of California, Santa Barbara, CA 93106 USA.

IEEE Log Number 9407785.

TABLE I

THE ELEMENTS OF $P_{\alpha\beta}$, $Q_{\alpha\beta}$, $L_{\alpha\beta}$ AND $M_{\alpha\beta}$ WHEN \mathbf{k} AXES ARE PARALLEL TO CUBIC AXES, I.E., $k_x//[100]$, $k_y//[010]$, AND $k_z//[001]$. EXPRESSIONS IN THE PARANTHESES ARE FOR $k_x//[1\bar{1}0]$, $k_y//[110]$, AND $k_z//[001]$ WHEN THEY DIFFER FROM THOSE FOR THE CUBIC AXES ORIENTATION. OTHERWISE, THE SAME EXPRESSION APPLIES FOR BOTH THE CRYSTAL ORIENTATIONS

$k_\alpha k_\beta$	k_x^2	k_y^2	k_z^2	$k_x k_y$	$k_x k_z$	$k_y k_z$
$P_{\alpha\beta}$	$\gamma_1 + \gamma_2$	$\gamma_1 + \gamma_2$	$\gamma_1 - 2\gamma_2$	0	0	0
$Q_{\alpha\beta}$	$\gamma_1 - \gamma_2$	$\gamma_1 - \gamma_2$	$\gamma_1 + 2\gamma_2$	0	0	0
$L_{\alpha\beta}$	0	0	0	0	$-2\sqrt{3}\gamma_3$	$-2\sqrt{3}i\gamma_3$
$M_{\alpha\beta}$	$\sqrt{3}\gamma_2$ ($\sqrt{3}\gamma_3$)	$-\sqrt{3}\gamma_2$ ($-\sqrt{3}\gamma_3$)	0	$-2\sqrt{3}i\gamma_3$ ($-2\sqrt{3}i\gamma_2$)	0	0

$$= \sum_{\alpha=x}^z \sum_{\beta=\alpha}^z \begin{bmatrix} P_{\alpha\beta} & L_{\alpha\beta} & M_{\alpha\beta} & 0 \\ L_{\alpha\beta}^\dagger & Q_{\alpha\beta} & 0 & M_{\alpha\beta} \\ M_{\alpha\beta}^\dagger & 0 & Q_{\alpha\beta} & -L_{\alpha\beta} \\ 0 & M_{\alpha\beta}^\dagger & -L_{\alpha\beta}^\dagger & P_{\alpha\beta} \end{bmatrix} k_\alpha k_\beta \quad (3)$$

$$\equiv \sum_{\alpha=x}^z \sum_{\beta=\alpha}^z \mathbf{H}_{\alpha\beta} k_\alpha k_\beta \quad (4)$$

where α and β are appropriate indices corresponding to coordinates x , y , or z . Equation (3) is nothing but decomposition of the original P , Q , L , and M elements into six terms, each one being the coefficient of k_x^2 , $k_x k_y$, $k_x k_z$, k_y^2 , $k_y k_z$, and k_z^2 terms. The elements of $P_{\alpha\beta}$, $Q_{\alpha\beta}$, $L_{\alpha\beta}$, and $M_{\alpha\beta}$ for typical crystal orientations are listed in Table I using the Luttinger parameters γ_1 , γ_2 , and γ_3 . The forms of these terms for the arbitrary crystal orientation can be determined by following the procedures given by Luttinger and Kohn [13], [15], [16].

$$\mathbf{J}_V = [J_1 \quad J_2 \quad J_3 \quad J_4]^T$$

are the envelope functions for the basis set [13] $\{|3/2, 3/2\rangle$, $\{|3/2, 1/2\rangle$, $\{|3/2, -1/2\rangle$, $\{|3/2, -3/2\rangle\}$.

A. Formulation for Quantum Wells

For x , y , and z along any crystal orientation, the Luttinger-Kohn Hamiltonian can be expressed in the form of (4). For a quantum-well structure, if one defines the growth direction as z -axis, k_z is to be replaced with $-i\partial/\partial z$. Then the \mathbf{H}_{LK} can be arranged into

$$\mathbf{H}_{LK} = \mathbf{H}_{zz} k_z^2 (\mathbf{H}_{xx} k_x + \mathbf{H}_{yz} k_y) k_z + (\mathbf{H}_{xx} k_x^2 + \mathbf{H}_{yy} k_y^2 + \mathbf{H}_{xy} k_x k_y) \quad (5)$$

$$\equiv \mathbf{H}_A k_z^2 + \mathbf{H}_B k_z + \mathbf{H}_C \quad (6)$$

$$= -\mathbf{H}_A \frac{\partial^2}{\partial z^2} - i\mathbf{H}_B \frac{\partial}{\partial z} + \mathbf{H}_C. \quad (7)$$

To ensure Hermiticity, (7) can be written as [16]

$$\mathbf{H}_{LK} \equiv -\frac{\partial}{\partial z} \mathbf{H}_A \frac{\partial}{\partial z} - i\frac{1}{2} \left(\mathbf{H}_B \frac{\partial}{\partial z} + \frac{\partial}{\partial z} \mathbf{H}_B \right) + \mathbf{H}_C. \quad (8)$$

The set of equations that need to be solved are given in (1). In order to be able to apply the FEM analysis, it is

desirable to find a variational expression corresponding to this set of coupled partial differential equations. This is not a straightforward procedure. To achieve this, an inner product of \mathbf{J}_v and the set of equations given in (1) is formed as

$$J = \langle \mathbf{J}_v | \mathbf{H}_{LK} + V(z) \mathbf{I} | \mathbf{J}_v \rangle - \langle \mathbf{J}_v | E | \mathbf{J}_v \rangle \quad (9)$$

$$= \int \mathbf{J}_v^\dagger \left[-\frac{\partial}{\partial z} \mathbf{H}_A \frac{\partial}{\partial z} - \frac{i}{2} \left(\mathbf{H}_B \frac{\partial}{\partial z} + \frac{\partial}{\partial z} \mathbf{H}_B \right) + \mathbf{H}_C + (V(z) - E) \mathbf{I} \right] \mathbf{J}_v dz. \quad (10)$$

Now an integration by parts is carried out, and the following equality is used to eliminate the remainder terms:

$$\left[\mathbf{H}_A^{(1)} \frac{\partial}{\partial z} + \frac{i}{2} \mathbf{H}_B^{(1)} \right] \mathbf{J}_v^{(1)} = \left[\mathbf{H}_A^{(2)} \frac{\partial}{\partial z} + \frac{i}{2} \mathbf{H}_B^{(2)} \right] \mathbf{J}_v^{(2)} \quad (11)$$

where the indices (1) and (2) represent region 1 and 2 across an interface. This equality actually results from the flux continuity across the interface and is equivalent to enforcing the boundary conditions on the continuity of the envelope functions across the interface [17]. They can be easily obtained by integrating (8) across the interface. Then one obtains the following variational expression:

$$J = \int \left[\left(\frac{\partial}{\partial z} \mathbf{J}_v^\dagger \right) \mathbf{H}_A \left(\frac{\partial}{\partial z} \mathbf{J}_v \right) + \frac{i}{2} \left\{ \left(\frac{\partial}{\partial z} \mathbf{J}_v^\dagger \right) \mathbf{H}_B \mathbf{J}_v - \mathbf{J}_v^\dagger \mathbf{H}_B \left(\frac{\partial}{\partial z} \mathbf{J}_v \right) \right\} \right] dz + \int \mathbf{J}_v^\dagger (\mathbf{H}_C + V(z)) \mathbf{J}_v dz - \int \mathbf{J}_v^\dagger E \mathbf{J}_v dz. \quad (12)$$

This can be proved by observing that (12) can be transformed back into the original Luttinger-Kohn Hamiltonian by applying the Euler equation of the variational principle [14]. The variational calculus states that the functional obtained this way is stationary around the correct solution. Therefore, the solution of the original Hamiltonian can be obtained by minimizing the functional given by (12). In this paper, a finite-element method is applied to achieve this numerically. In this approach, one expresses the envelope functions over a mesh

as $\mathbf{J}_v = \mathbf{N}(z)\mathbf{F}$, where \mathbf{N} is a shape function of each line element, and \mathbf{F} is a column vector whose elements are its nodal values [18]. Making this discretization reduces the functional that needs to be minimized to a matrix equation as shown below

$$J = \mathbf{F}^\dagger \left[\int \left\{ \frac{\partial \mathbf{N}^T}{\partial z} \mathbf{H}_A \frac{\partial \mathbf{N}}{\partial z} + \frac{i}{2} \left(\frac{\partial \mathbf{N}^T}{\partial z} \mathbf{H}_B \mathbf{N} - \mathbf{N}^T \mathbf{H}_B \frac{\partial \mathbf{N}}{\partial z} \right) \right\} dz \right] \mathbf{F} + \mathbf{F}^\dagger \left[\int \mathbf{N}^T (\mathbf{H}_C + V(z)) \mathbf{N} dz \right] \mathbf{F} - E \mathbf{F}^\dagger \left[\int \mathbf{N}^T \mathbf{N} dz \right] \mathbf{F} \quad (13)$$

$$\equiv \mathbf{F}^\dagger \mathbf{K} \mathbf{F} - E \mathbf{F}^\dagger \mathbf{M} \mathbf{F} \quad (14)$$

where \mathbf{K} is a Hamiltonian matrix corresponding to the first and the second terms, and \mathbf{M} is a matrix corresponding to the last term in (13), respectively. Since this expression should be stationary around the correct solution, its variation with respect to the unknown nodal values should be zero, which yields

$$\frac{\partial J}{\partial \mathbf{F}^\dagger} = \mathbf{0} = \mathbf{K} \mathbf{F} - E \mathbf{M} \mathbf{F}. \quad (15)$$

This is an eigenvalue equation for the unknown energy eigenvalues and wavefunctions. Therefore, by solving this problem, the energy eigenvalue, E , and the numerical values of the wavefunctions at the nodes of the mesh, which are the elements of \mathbf{F} , can be obtained. Usually, \mathbf{K} and \mathbf{M} are sparse banded Hermitian matrices, hence this problem can be solved very efficiently using the subspace iteration algorithm and Rayleigh quotient method with LU decomposition algorithm for sparse banded matrices [19].

B. Formulation for Quantum Wires

For a quantum-wire structure with wire parallel to k_x direction, k_y and k_z can be replaced with $-i\partial/\partial y$ and $-i\partial/\partial z$, respectively [3]. Then the \mathbf{H}_{LK} in (4) leads to

$$\mathbf{H}_{LK} = \mathbf{H}_{yy} k_y^2 + \mathbf{H}_{xy} k_x k_y + \mathbf{H}_{zz} k_z^2 + \mathbf{H}_{xz} k_x k_z + \mathbf{H}_{yz} k_y k_z + \mathbf{H}_{xx} k_x^2 \quad (16)$$

$$= -\mathbf{H}_{yy} \frac{\partial^2}{\partial y^2} - ik_x \mathbf{H}_{xy} \frac{\partial}{\partial y} - \mathbf{H}_{zz} \frac{\partial^2}{\partial z^2} - ik_x \mathbf{H}_{xz} \frac{\partial}{\partial z} - \mathbf{H}_{yz} \frac{\partial}{\partial y} \frac{\partial}{\partial z} + \mathbf{H}_{xx} k_x^2. \quad (17)$$

To ensure Hermiticity, (17) can be written as

$$\mathbf{H}_{LK} \equiv -\frac{\partial}{\partial y} \mathbf{H}_{yy} \frac{\partial}{\partial y} - \frac{ik_x}{2} \left(\mathbf{H}_{xy} \frac{\partial}{\partial y} + \frac{\partial}{\partial y} \mathbf{H}_{xy} \right) - \frac{\partial}{\partial z} \mathbf{H}_{zz} \frac{\partial}{\partial z} - \frac{ik_x}{2} \left(\mathbf{H}_{xz} \frac{\partial}{\partial z} + \frac{\partial}{\partial z} \mathbf{H}_{xz} \right) - \frac{1}{2} \left(\frac{\partial}{\partial y} \mathbf{H}_{yz} \frac{\partial}{\partial z} + \frac{\partial}{\partial z} \mathbf{H}_{yz} \frac{\partial}{\partial y} \right) + \mathbf{H}_{xx} k_x^2. \quad (18)$$

As described in the previous section, the functional that is stationary around the solution of the differential equation is found by forming an inner product as shown below:

$$J = \langle \mathbf{J}_v | \mathbf{H}_{LK} + V(y, z) \mathbf{I} | \mathbf{J}_v \rangle - \langle \mathbf{J}_v | E | \mathbf{J}_v \rangle = \iint \mathbf{J}_v^\dagger \left[-\frac{\partial}{\partial y} \mathbf{H}_{yy} - \frac{\partial}{\partial z} \mathbf{H}_{zz} \frac{\partial}{\partial z} - \frac{1}{2} \left(\frac{\partial}{\partial y} \mathbf{H}_{yz} \frac{\partial}{\partial z} + \frac{\partial}{\partial z} \mathbf{H}_{yz} \frac{\partial}{\partial y} \right) - \frac{ik_x}{2} \left(\mathbf{H}_{xy} \frac{\partial}{\partial y} + \frac{\partial}{\partial y} \mathbf{H}_{xy} + \mathbf{H}_{xz} \frac{\partial}{\partial z} + \frac{\partial}{\partial z} \mathbf{H}_{xz} \right) + \mathbf{H}_{xx} k_x^2 + (V(y, z) - E) \mathbf{I} \right] \mathbf{J}_v dy dz. \quad (19)$$

Again, an integration by parts is carried out and the remaining terms are eliminated using the following equations:

$$\left[\mathbf{H}_{yy}^{(1)} \frac{\partial}{\partial y} + \frac{1}{2} \mathbf{H}_{yz}^{(1)} \frac{\partial}{\partial z} + \frac{ik_x}{2} \mathbf{H}_{xy}^{(1)} \right] \mathbf{J}_v^{(1)} = \left[\mathbf{H}_{yy}^{(2)} \frac{\partial}{\partial y} + \frac{1}{2} \mathbf{H}_{yz}^{(2)} \frac{\partial}{\partial z} + \frac{ik_x}{2} \mathbf{H}_{xy}^{(2)} \right] \mathbf{J}_v^{(2)} \quad (20)$$

across an interface normal to y -axis, and

$$\left[\mathbf{H}_{zz}^{(1)} \frac{\partial}{\partial z} + \frac{1}{2} \mathbf{H}_{yz}^{(1)} \frac{\partial}{\partial y} + \frac{ik_x}{2} \mathbf{H}_{xz}^{(1)} \right] \mathbf{J}_v^{(1)} = \left[\mathbf{H}_{zz}^{(2)} \frac{\partial}{\partial z} + \frac{1}{2} \mathbf{H}_{yz}^{(2)} \frac{\partial}{\partial y} + \frac{ik_x}{2} \mathbf{H}_{xz}^{(2)} \right] \mathbf{J}_v^{(2)} \quad (21)$$

across an interface normal to z -axis. These equations result from the boundary conditions on the envelope functions across the interface and can easily be obtained by integrating (18) across the interfaces normal to y and z -axes. Then one obtains the following variational expressions:

$$J = \int \int \left[\frac{\partial \mathbf{J}_v^\dagger}{\partial y} \mathbf{H}_{yy} \frac{\partial \mathbf{J}_v}{\partial y} + \frac{\partial \mathbf{J}_v^\dagger}{\partial z} \mathbf{H}_{zz} \frac{\partial \mathbf{J}_v}{\partial z} + \frac{1}{2} \left(\frac{\partial \mathbf{J}_v^\dagger}{\partial y} \mathbf{H}_{yz} \frac{\partial \mathbf{J}_v}{\partial z} + \frac{\partial \mathbf{J}_v^\dagger}{\partial z} \mathbf{H}_{yz} \frac{\partial \mathbf{J}_v}{\partial y} \right) - \frac{ik_x}{2} \left(\mathbf{J}_v^\dagger \mathbf{H}_{xy} \frac{\partial \mathbf{J}_v}{\partial y} - \frac{\partial \mathbf{J}_v^\dagger}{\partial y} \mathbf{H}_{xy} \mathbf{J}_v + \mathbf{J}_v^\dagger \mathbf{H}_{xz} \frac{\partial \mathbf{J}_v}{\partial z} - \frac{\partial \mathbf{J}_v^\dagger}{\partial z} \mathbf{H}_{xz} \mathbf{J}_v \right) \right] dy dz + \int \int \mathbf{J}_v^\dagger \left(k_x^2 \mathbf{H}_{xx} + (V(y, z) - E) \mathbf{I} \right) \mathbf{J}_v dy dz. \quad (22)$$

Again, one can verify that this functional yields the original set of equations through the Euler equation [14]. To apply the finite-element method, one expresses the envelope functions as $\mathbf{J}_v = \mathbf{N}(y, z)\mathbf{F}$, where $\mathbf{N}(y, z)$ is a two-dimensional shape function of each triangular element, and \mathbf{F} is a column vector of its nodal values [20]. This form reduces the functional into

a matrix equation as shown below

$$\begin{aligned}
 J = \mathbf{F}^\dagger & \left[\int \int \left\{ \frac{\partial \mathbf{N}^T}{\partial y} \mathbf{H}_{yy} \frac{\partial \mathbf{N}}{\partial y} + \frac{\partial \mathbf{N}^T}{\partial z} \mathbf{H}_{zz} \frac{\partial \mathbf{N}}{\partial z} \right. \right. \\
 & + \frac{1}{2} \left(\frac{\partial \mathbf{N}^T}{\partial y} \mathbf{H}_{yz} \frac{\partial \mathbf{N}}{\partial z} + \frac{\partial \mathbf{N}^T}{\partial z} \mathbf{H}_{yz} \frac{\partial \mathbf{N}}{\partial y} \right) \\
 & - \frac{ik_x}{2} \left(\mathbf{N}^T \mathbf{H}_{xy} \frac{\partial \mathbf{N}}{\partial y} - \frac{\partial \mathbf{N}^T}{\partial y} \mathbf{H}_{xy} \mathbf{N} + \mathbf{N}^T \mathbf{H}_{xz} \frac{\partial \mathbf{N}}{\partial z} \right. \\
 & \left. \left. - \frac{\partial \mathbf{N}^T}{\partial z} \mathbf{H}_{xz} \mathbf{N} \right) \right\} dy dz \Big] \mathbf{F} \\
 & + \mathbf{F}^\dagger \left[\int \int \mathbf{N}^T (k_x^2 \mathbf{H}_{xx} + V(y, z) \mathbf{I}) \mathbf{N} dy dz \right] \mathbf{F} \\
 & - E \mathbf{F}^\dagger \left[\int \int \mathbf{N}^T \mathbf{N} dy dz \right] \mathbf{F} \quad (23)
 \end{aligned}$$

$$\equiv \mathbf{F}^\dagger \mathbf{K} \mathbf{F} - E \mathbf{F}^\dagger \mathbf{M} \mathbf{F} \quad (24)$$

where \mathbf{K} corresponds to the first and the second terms, and \mathbf{M} corresponds to the last term in (23), respectively. Using the variational nature of this equation, it is reduced to an equation as $\mathbf{K} \mathbf{F} = E \mathbf{M} \mathbf{F}$ as described earlier.

C. Comparison to Other Published Results

After this formulation, two test cases were solved to check the accuracy of the approach. These are a GaAs quantum well and a GaAs quantum wire for which k_x , k_y , and k_z are parallel to the cubic axes. The barrier material is $\text{Al}_{0.2}\text{Ga}_{0.8}\text{As}$ in the both cases. The results are shown in Table II together with the results of two other approaches, namely, the finite-difference method (FDM) [10] and the effective bond-orbital model (EBOM) [11]. For the FDM, the coupled set of partial differential equations are solved directly using a finite difference discretization for the partial derivatives. The EBOM exploits the symmetry of the problem and uses a variational approach. The valence band potential barrier height is assumed to be 98 meV, and the Luttinger parameters are assumed to be constant at $\gamma_1 = 6.85$, $\gamma_2 = 2.1$, and $\gamma_3 = 2.9$, as used in [11] to make a fair comparison. When $k_x // (100)$, $k_y // (010)$, and $k_z // (001)$, the coefficients of the matrices \mathbf{K} for the quantum well case are as follows:

$$\mathbf{K} = \int \mathbf{H}_{qw} dz \equiv \int \begin{bmatrix} P_{qw} & L_{qw} & M_{qw} & 0 \\ L_{qw}^\dagger & Q_{qw} & 0 & M_{qw} \\ M_{qw}^\dagger & 0 & Q_{qw} & -L_{qw} \\ 0 & M_{qw}^\dagger & -L_{qw}^\dagger & P_{qw} \end{bmatrix} dz \quad (25)$$

where

$$\begin{aligned}
 P_{qw} &= (\gamma_1 + \gamma_2)(k_x^2 \mathbf{N}^T \mathbf{N} + k_y^2 \mathbf{N}^T \mathbf{N}) \\
 &+ (\gamma_1 - 2\gamma_2) \frac{\partial \mathbf{N}^T}{\partial z} \frac{\partial \mathbf{N}}{\partial z} + V(z) \mathbf{N}^T \mathbf{N} \\
 Q_{qw} &= (\gamma_1 - \gamma_2)(k_x^2 \mathbf{N}^T \mathbf{N} + k_y^2 \mathbf{N}^T \mathbf{N}) \\
 &+ (\gamma_1 + 2\gamma_2) \frac{\partial \mathbf{N}^T}{\partial z} \frac{\partial \mathbf{N}}{\partial z} + V(z) \mathbf{N}^T \mathbf{N}
 \end{aligned}$$

$$L_{qw} = -\sqrt{3}\gamma_3(k_x - ik_y) \left(\mathbf{N}^T \frac{\partial \mathbf{N}}{\partial z} - \frac{\partial \mathbf{N}^T}{\partial z} \mathbf{N} \right)$$

$$M_{qw} = \{ \sqrt{3}\gamma_2(k_x^2 - k_y^2) - 2\sqrt{3}\gamma_3 ik_x k_y \} \mathbf{N}^T \mathbf{N}$$

whereas for the quantum-wire case,

$$\begin{aligned}
 \mathbf{K} &= \int \int \mathbf{H}_{qwr} dy dz \\
 &\equiv \int \int \begin{bmatrix} P_{qwr} & L_{qwr} & M_{qwr} & 0 \\ L_{qwr}^\dagger & Q_{qwr} & 0 & M_{qwr} \\ M_{qwr}^\dagger & 0 & Q_{qwr} & -L_{qwr} \\ 0 & M_{qwr}^\dagger & -L_{qwr}^\dagger & P_{qwr} \end{bmatrix} dy dz \quad (26)
 \end{aligned}$$

where

$$P_{qwr} = (\gamma_1 + \gamma_2) \left(k_x^2 \mathbf{N}^T \mathbf{N} + \frac{\partial \mathbf{N}^T}{\partial y} \frac{\partial \mathbf{N}}{\partial y} \right)$$

$$+ (\gamma_1 - 2\gamma_2) \frac{\partial \mathbf{N}^T}{\partial z} \frac{\partial \mathbf{N}}{\partial z} + V(y, z) \mathbf{N}^T \mathbf{N}$$

$$Q_{qwr} = (\gamma_1 - \gamma_2) \left(k_x^2 \mathbf{N}^T \mathbf{N} + \frac{\partial \mathbf{N}^T}{\partial y} \frac{\partial \mathbf{N}}{\partial y} \right)$$

$$+ (\gamma_1 + 2\gamma_2) \frac{\partial \mathbf{N}^T}{\partial z} \frac{\partial \mathbf{N}}{\partial z} + V(y, z) \mathbf{N}^T \mathbf{N}$$

$$L_{qwr} = -\sqrt{3}\gamma_3 k_x \left(\mathbf{N}^T \frac{\partial \mathbf{N}}{\partial z} - \frac{\partial \mathbf{N}^T}{\partial z} \mathbf{N} \right)$$

$$- \sqrt{3}\gamma_3 \left(\frac{\partial \mathbf{N}^T}{\partial y} \frac{\partial \mathbf{N}}{\partial z} + \frac{\partial \mathbf{N}^T}{\partial z} \frac{\partial \mathbf{N}}{\partial y} \right)$$

$$M_{qwr} = \sqrt{3}\gamma_2 \left(k_x^2 \mathbf{N}^T \mathbf{N} - \frac{\partial \mathbf{N}^T}{\partial y} \frac{\partial \mathbf{N}}{\partial y} \right)$$

$$- \sqrt{3}\gamma_3 k_x \left(\mathbf{N}^T \frac{\partial \mathbf{N}}{\partial y} - \frac{\partial \mathbf{N}^T}{\partial y} \mathbf{N} \right).$$

\mathbf{M} is a block diagonal matrix, i.e.,

$$\mathbf{M} \equiv \begin{bmatrix} \mathbf{M}_{\text{dia}} & \mathbf{0} & \mathbf{0} & \mathbf{0} \\ \mathbf{0} & \mathbf{M}_{\text{dia}} & \mathbf{0} & \mathbf{0} \\ \mathbf{0} & \mathbf{0} & \mathbf{M}_{\text{dia}} & \mathbf{0} \\ \mathbf{0} & \mathbf{0} & \mathbf{0} & \mathbf{M}_{\text{dia}} \end{bmatrix} \quad (27)$$

where

$$\mathbf{M}_{\text{dia}} = \int \mathbf{N}^T \mathbf{N} dz \quad \text{or} \quad \mathbf{M}_{\text{dia}} = \int \int \mathbf{N}^T \mathbf{N} dy dz \quad (28)$$

for the quantum-well case and quantum-wire case, respectively. The results in Table II indicate that the FEM approach coupled with the variational formulation gives the same result when the original Hamiltonian is solved using the FDM as well as by another independent approach. Along with the accuracy, another potential important advantage of FEM is that it can be applied to arbitrarily shaped inhomogeneous quantum confined structures like the tilted and serpentine superlattices without additional effort such as coordinate transformations. Furthermore, the mesh size does not have to be uniform hence it is possible to model a region of interest with as many elements as needed in order to represent the physical behavior accurately. For the particular case reported in Table II, the

TABLE II
THE VALENCE BAND ZONE CENTER ENERGIES IN meV FOR (a) A $100 \text{ \AA} \times 100 \text{ \AA}$ SQUARE QUANTUM WIRE AND FOR (b) A 100 \AA QUANTUM WELL WITH $\gamma_1 = 6.85$, $\gamma_2 = 2.1$, $\gamma_3 = 2.9$, $\Delta = \infty$, AND $V = 98 \text{ meV}$. THE GRID SIZE IS 40×40 , RESULTING IN A TOTAL OF 1600 NODAL VALUES IN BOTH FEM AND FDM

subband	(a) QWR			(b) QW	
	FEM	FDM	EBOM ¹¹	FEM	EBOM ¹¹
1	17.13	17.00	17.1	6.88	6.9
2	28.21	27.79	28.1	20.36	20.4
3	28.41	28.10	28.5	27.15	27.7
4	38.59	38.15	38.4	59.31	59.7
5	51.35	51.09	50.8	73.91	73.9

grid size is 40×40 , resulting in a total of 1600 nodal values. Since there are 4 envelope functions, the K and M matrices in equations (26) and (27) are 6400×6400 square matrices. They are about 20 times smaller than those of EBOM [11] and TBM [12], which provides a substantial advantage in the required computational effort.

Another case that is quite important and deserves particular attention is a superlattice of quantum wires, i.e., a quantum-wire array. In this case, potential profile usually has a periodicity and one can simplify the problem using the Bloch theorem. This states that the wavefunction in one cell is exactly the same as that in the adjacent cell, except for phase term of e^{-jkD} , where k is the Bloch wavenumber and D is the period. In other words, $F(y + D, z) = F(y, z)e^{-ikD}$, where y -axis is parallel to the array direction, z -axis is perpendicular to the plane of the wire array, and x -axis is parallel to the wires. With this periodic boundary condition [21], an infinite array of QWR can be analyzed and their $E - k$ diagram can be calculated. Once this is done, one can derive the density of states function and gain characteristics of the array.

III. ANALYSIS OF TILTED AND SERPENTINE SUPERLATTICES

The schematic cross-sectional profiles of the tilted superlattice (TSL) and serpentine superlattice (SSL) that are investigated in this work are shown in Fig. 1. The TSL and SSL are grown on (001) GaAs vicinal substrates tilted toward [110] direction by an angle α . Under the right growth conditions, a uniform atomic staircase on the vicinal substrate is formed, and one can grow an array of quantum wires parallel to the $[1\bar{1}0]$ direction [4], [6]. Then the period of the superlattice is determined by the monolayer thickness, d , and surface tilt angle, α , as $D = d/\tan(\alpha)$. For example, when $\alpha = 2^\circ$, $D = 81 \text{ \AA}$, and when $\alpha = 1.5^\circ$, $D = 108 \text{ \AA}$. In this section, the conduction and valence subband dispersions of TSL and SSL will be calculated and compared to that of the quantum-well structures.

A. Electronic Band Structure

Fig. 2 shows the conduction and valence energy band diagrams of a 100-\AA -thick GaAs-Al_{0.2}Ga_{0.8}As quantum well. The bulk bandgaps and Luttinger parameters used in the

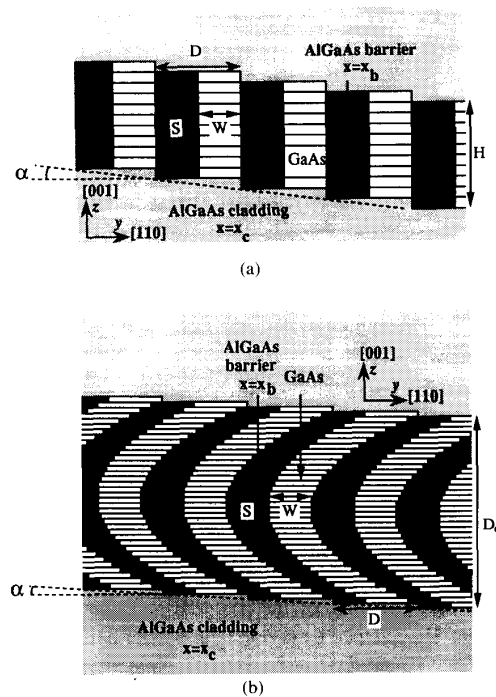


Fig. 1. Schematic cross-sectional profile of lateral superlattices investigated in this work. (a) Tilted superlattice (TSL). (b) Serpentine superlattice (SSL).

calculations are given in Table III. A conduction-band offset of 57% was assumed [22] for the AlGaAs system. The conduction band dispersion is almost parabolic in [100] and [110] directions since only one band effective mass Hamiltonian was used in its analysis. The corresponding density of states (DOS) in the conduction band also is plotted on the same figure and shows steps [23] of height $m_n^*/\pi\hbar^2 L_z$ where m_n^* is the effective mass of n th conduction subband [24] and L_z is the quantum-well thickness. For the valence subbands, a strong nonparabolicity is observed indicating band mixing effects [11], [25], [26]. Consequently, the resulting DOS is quite different from a step-like profile. Its overall magnitude is also larger than that of the conduction band by an order of magnitude, which hinders achieving transparency and

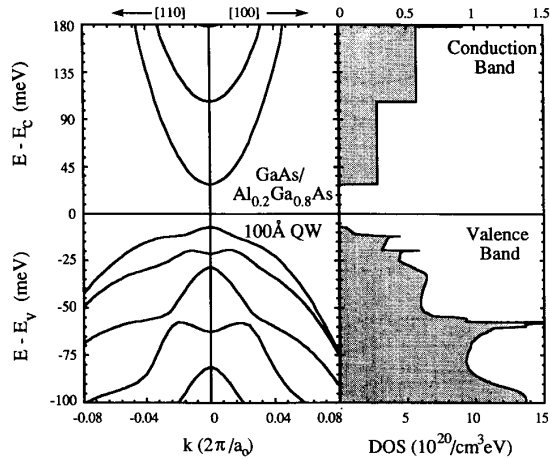


Fig. 2. Conduction and valence energy band diagram of a 100-Å-thick GaAs-Al_{0.2}Ga_{0.8}As quantum well. At right is the corresponding density of states (DOS) function. Note that the scale for the conduction band (CB) DOS is 10 times smaller than the valence band (VB) DOS scale, a_0 is the lattice constant for GaAs.

TABLE III
Al_xGa_{1-x}As MATERIAL PARAMETERS USED IN THE CALCULATIONS OF THIS STUDY. THE CONDUCTION-BAND OFFSET IS TAKEN AS 57% OF BANDGAP CHANGE [22]

Bulk band gap ³⁸ (eV)	$E_g(x)=1.424+1.721x-1.437x^2+1.310x^3$
Luttinger parameters ³⁹	$\gamma_1(x)=6.85(1-x)+3.45x$ $\gamma_2(x)=2.1(1-x)+0.68x$ $\gamma_3(x)=2.9(1-x)+1.29x$ $m_c(x)=0.0667(1-x)+0.15x$

threshold for lasing at low current densities [26]. Moreover, the energy separation between the lowest two valence subbands is less than 10 meV.

In Fig. 3, the results of energy band calculations and DOS of a tilted superlattice are shown. The rectangular wire array is 100-Å thick and 40.5-Å wide with a 40.5-Å separation between wires, which are the typical values for 2° off TSL. The wire material is GaAs, the barrier material is Al_{0.5}Ga_{0.5}As, and cladding material is Al_{0.4}Ga_{0.6}As. In a TSL, the atomic steps run parallel to [1 $\bar{1}$ 0] direction [4]. Therefore, the wires are along [1 $\bar{1}$ 0] direction and are equally spaced along [110] direction, which is defined as the array direction. Due to close proximity of the wires, there is a certain amount of coupling. This broadens the subbands of the wires into minibands. As a result, in array direction, a certain amount of subband dispersion is observed. The energy widths of these minibands are smaller for lower subbands since the corresponding wavefunctions are more tightly confined for the lower subbands, reducing the coupling between wires. Fig. 4 shows the contour plots of the electron wavefunction magnitude at the zone center

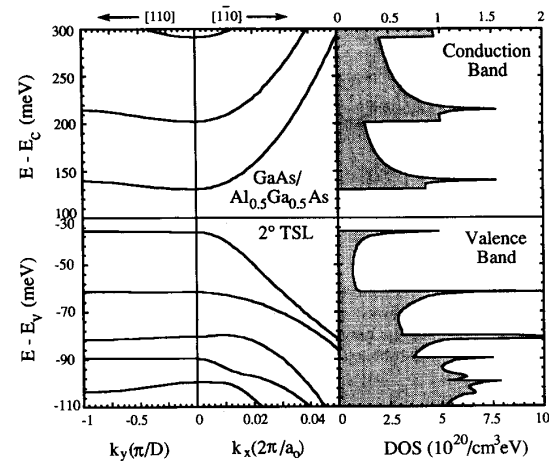


Fig. 3. Conduction and valence energy band diagram of a 100-Å thick GaAs-Al_{0.5}Ga_{0.5}As tilted superlattice quantum-wire array on a 2° off vicinal substrate ($W = S = 40.5$ Å). Other parameters are given in the text. Quantum wires are parallel to [1 $\bar{1}$ 0] direction are equally spaced along [110] direction. At right is the corresponding density of states function. The scale for the CB DOS is 5 times smaller than the VB DOS scale.

for the two lowest conduction subbands, substantiating this argument. The corresponding DOS functions are shown on the right side of Fig. 3. For a single wire or a wire array with infinite barrier potentials, the DOS would show sharp peaks at the subband minima due to inverse square root of energy dependence of ideal quantum-wire DOS [23]. However, due to a finite width of the minibands, the real DOS function shows step-like behavior at the miniband minima and sharp peaks at the miniband maxima. The step height at the subband minimum is proportional to $\sqrt{m_w m_a} / \pi \hbar^2 L_z$ as shown in the Appendix. In this expression, m_w is the effective mass along the wire direction, i.e., [1 $\bar{1}$ 0] direction, and m_a is the effective mass along the array direction, i.e., [110] direction. Even though any quantum wire array DOS will have a sharp peak at the miniband top due to enhanced effective mass, this peak which has a narrow width does not play a significant role in gain enhancement due to the line broadening [27]. On the other hand, an increase of the step height at the subband minimum is more important for gain enhancement. As a matter of fact, the gain enhancement that will result in using a quantum-wire array with some coupling between the wires compared to a quantum well can be estimated based on the ratio of the DOS step heights of these two structures at the conduction band minima. For this particular TSL structure, the step height of the lowest conduction band DOS function is almost 3 times higher than that of the 100-Å thick quantum well discussed earlier. The corresponding gain curves will also differ by about the same ratio, as will be shown and discussed later in connection with Fig. 8.

Since the hole effective mass is higher than the electron effective mass, the wire-to-wire coupling in the valence band is almost negligible and the width of the miniband is very small. The subbands are twofold degenerate as in the quantum-well case since the TSL structure under consideration has inversion symmetry. For the lower subbands, the corresponding DOS

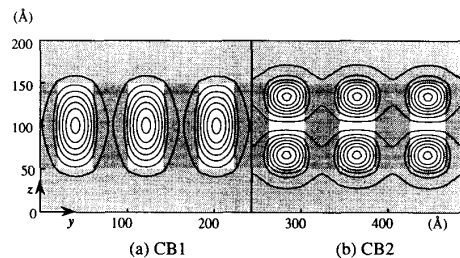


Fig. 4. Contour plots of the electron envelope wavefunction magnitude at zone center for the two lowest conduction band eigenstates of the TSL studied in this work. The contours range from 5% to 95% with 15% increments. For the second conduction subband (CB2) significant coupling between quantum wires is observed.

is almost like that of an ideal quantum wire. The overall magnitude of DOS is also comparable to that of conduction band. The separation between the lowest subbands is about 25 meV in valence band 70 meV in conduction band. These large subband separation and sharp DOS profile promise an enhanced gain.

Although the ideal TSL structure is quite promising, there is a practical difficulty in the fabrication of a TSL, which was recognized early on [4]. To keep the interface between the barriers and wires vertical, one has to know the exact growth rate of each material and keep them constant throughout the growth [4]. Any deviation from the correct value would tilt this interface, and hence will distort the quantum-wire geometry. This difficulty can be circumvented if one deliberately varies the growth rate from less than the correct value to greater than the correct value [6]. Then one grows a superlattice with curved growth interfaces as shown in Fig. 1(b), and somewhere within the grown layer where the interface between the wire and the barrier material is vertical, i.e., when the effective width of barrier is the largest, one obtains a two-dimensional confinement. Fig. 5 shows the results of energy band and DOS calculations for a serpentine superlattice. For a linear growth rate variation, the interface between the wire and barrier material can be expressed as [6] $y = Kz^2$, where $K = 2\Delta p/d_0 \tan \alpha$. In this expression, Δp is the ratio of the maximum deviation in the linear growth rate variation to its nominal value, d_0 is the thickness of the superlattice, and α is the substrate tilt angle [4]. In this particular case, $D_0 = 230 \text{ \AA}$, $\alpha = 2^\circ$ and $\Delta p = 0.10$, implying $K = 1/40 \text{ \AA}$. Due to the high curvature of the interfaces, the quantum confinement of the lowest subband is strong and the envelope function is localized in the central part of the superlattice as shown in Fig. 6(a). Nevertheless, there is a miniband with a small width due to close proximity of the wires. For the higher subbands, however, the wavefunction extends outside the low bandgap wire material, as shown in Fig. 6(b). So for the higher conduction subbands, the coupling between wires becomes significant and they have wide miniband widths. As a result, the height of the step in the DOS is relatively small. The lowest valence subbands are well confined within the quantum-wire regions, regardless of heavy hole-like or light hole-like character of the subbands, as shown in Fig. 6(c) and (d). Hence, the coupling between wires is small and the dispersion

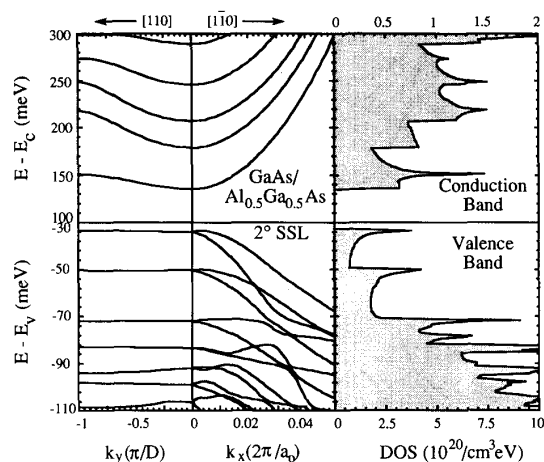


Fig. 5. Conduction and valence energy band diagram of a GaAs- $\text{Al}_{0.5}\text{Ga}_{0.5}\text{As}$ serpentine superlattice quantum-wire array on a 2° off vicinal substrate ($\Gamma = S = 40.5 \text{ \AA}$). Other parameters are given in the text. Quantum wires are parallel to $[1\bar{1}0]$ direction and are equally spaced along $[110]$ direction. At right is the corresponding density of states function. The scale for the CB DOS is 5 times smaller than the VB DOS scale.

along the array direction is almost negligible. As a result, the valence band DOS is ideal quantum wire-like. The separation between the two lowest subbands is 17 meV in valence band, while it is 45 meV in the conduction band. Along the wire direction, except at the zone center, the twofold degeneracy no longer exists due to the lack of inversion symmetry in the geometry. At the zone center, the first subband has heavy hole character, because the heavy hole basis functions have much larger amplitude than the light hole basis functions. The opposite is observed for the second subband, and this subband has mostly light hole like character at the zone center. Although it is possible to determine whether each subband is heavy hole-like or light hole-like, a significant amount of intermixing between heavy hole and light hole character was observed in the higher subbands. Such a complicated nature of the band intermixing strongly affects the momentum matrix element for optical transitions, which will be discussed in the next section.

B. Momentum Matrix Element for Optical Transitions

One of the important properties of a quantum wire is highly anisotropic momentum matrix element. This offers the possibility of obtaining enhanced gain along particular directions [28]–[30]. But in a practical quantum-wire array, it is very difficult to predict the magnitude of the momentum matrix element analytically due to the band mixing effects and the differences in the sizes of confinement between conduction and valence bands. Therefore, a numerical approach is needed. In the FEM analysis, the envelope wavefunctions are obtained simultaneously with the energy values. Therefore, one can construct the wavefunctions for each state using envelope functions and basis functions, and numerically obtain the momentum matrix elements [3].

In Fig. 7, the momentum matrix elements for the QW, TSL, and SSL structures considered in this work are plotted in polar

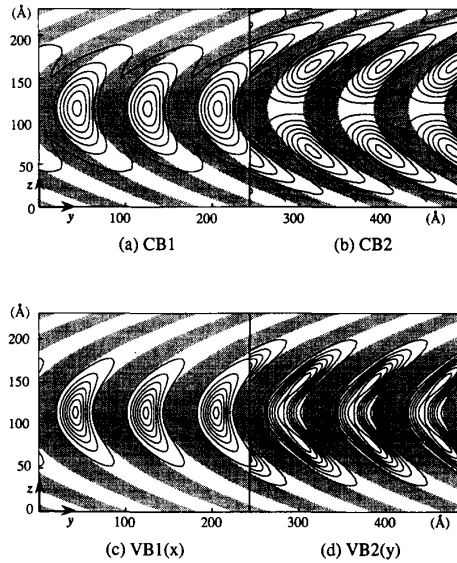


Fig. 6. The contour plots of the electron and hole envelope wavefunction magnitude at zone center for an SSL (a) for the lowest conduction subband, (b) for the second conduction subband, (c) for the lowest valence subband (only the envelope function for the $X \uparrow$ and $X \downarrow$ basis functions are shown, since they are dominant for this band at zone center), and (d) for the second valence subband (only the envelope function for the $Y \uparrow$ and $Y \downarrow$ basis functions are shown, since they are dominant for this band at zone center). The contours range from 5% to 95% with 15% increments. For conduction subbands, there is coupling between wires, whereas for the valence subbands, coupling is negligible due to heavier hole effective mass.

form. The numerical values of the momentum matrix elements for specific optical polarization directions are listed in Table IV. For the quantum well, C1-V1 transition, or heavy hole transition, is maximum when the optical polarization is in-plane, and minimum when it is perpendicular to the quantum-well plane. For C1-V2 transition, or light hole transition, the opposite is true, i.e., the momentum matrix element is maximum when the optical polarization is perpendicular to the quantum-well plane and minimum when it is in-plane. For the quantum-wire arrays considered in this work, i.e., either for TSL or SSL, the C1-V1 transition has mostly heavy hole-like character at zone center. The momentum matrix element for this transition is maximum when the optical polarization is along the wire direction, and is almost zero when the optical polarization is parallel to the shorter dimension of the quantum-wire cross section. The C1-V2 transition in TSL corresponds to the heavy hole-like transition. The C1-V3 transition in TSL, and C1-V2 transition in SSL, have mostly light hole-like character at zone center, and their momentum matrix elements have similar behavior. For the case of the light hole-like transition, the momentum matrix element is maximum when the optical polarization is along the shorter dimension of the wire-cross section. For TSL, it is minimum when the optical polarization is along the wires; while for SSL, it is minimum when the optical polarization is along the longer dimension of the wire cross section. These trends agree with qualitative understanding of band-to-band optical transitions in compound semiconductors [30], [31]. In general,

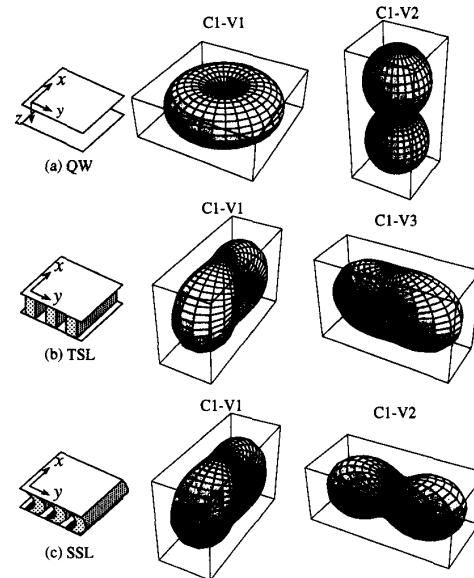


Fig. 7. Polar plots of the momentum matrix element for QW, TSL, and SSL considered in this work. The length of a line between the origin and a particular point on the surface corresponds to the magnitude of the momentum matrix element. The direction of the line connecting the origin to a particular point on the surface corresponds to the direction of the electric field of the interacting radiation, i.e., it defines the polarization of the light. Quantum wires are along $[1\bar{1}0]$ direction (x -axis) and the arrays are distributed along $[110]$ direction (y -axis).

the heavy hole-like subband has the maximum momentum matrix element when the optical polarization is parallel to a direction along which there is no quantum confinement, and minimum when the optical polarization is along the strongest quantum confinement direction. The opposite is true for the light hole-like subband for the TSL. In SSL, however, the minimum momentum matrix element is observed when optical polarization is parallel to the longer dimension of the lateral quantum confinement. This may be due to the fact that in SSL there is stronger band intermixing due to the higher curvature of the interfaces. Such valence band mixing effects become more significant in the higher subbands and are observed even at the zone center. Outside the zone center, the momentum matrix elements become more complicated, and in some cases a heavy hole-like subband turns into a light hole-like subband, and vice versa [29], [30].

Due to the different effective masses and potential barrier heights in conduction and valence bands, the envelope function in each band does not overlap completely; so the actual momentum matrix element tends to be smaller than the value obtained through ideal quantum-wire calculations, especially in the higher subbands. This trend is more significant for the weakly confined structures [32] and for the light hole-like transitions in quantum-wire arrays when the band mixing effect is strong. Therefore, for the realistic analysis of the optical properties of quantum wires, the actual momentum matrix elements should be calculated using the realistic wavefunctions in the conduction and valence bands, and other simple models like single band approximation or infinite barrier potential model may be very inaccurate [12], [26].

TABLE IV
NUMERICAL VALUES OF MOMENTUM MATRIX ELEMENT OF THE QW, TSL, AND
SSL STRUCTURES STUDIED IN THIS WORK FOR DIFFERENT POLARIZATION
DIRECTIONS. THE ACTUAL GEOMETRIES ARE DESCRIBED IN THE TEXT

Structure	Subbands involved in the transition	Direction of optical polarization		
		$x/[1\bar{1}0]$	$y/[110]$	$z/[001]$
QW	C1-V1 (heavy-hole)	0.97	0.97	0.0
	C1-V2 (light-hole)	0.33	0.33	1.33
	C2-V3 (heavy-hole)	0.86	0.86	0.0
	C2-V4 (light-hole)	0.33	0.33	1.33
TSL	C1-V1 (heavy-hole)	1.03	0.04	0.63
	C2-V2 (heavy-hole)	0.84	0.29	0.15
	C1-V3 (light-hole)	0.01	0.31	0.20
	C2-V4 (light-hole)	0.04	0.09	0.23
SSL	C1-V1 (heavy-hole)	0.86	0.03	0.55
	C1-V2 (light-hole)	0.13	0.34	0.05
	C2-V2 (heavy-hole)	0.51	0.09	0.17
	C2-V3 (light-hole)	0.04	0.21	0.06

C. Optical Gain

By combining the density of states function and the momentum matrix elements, one can obtain optical gain characteristics of the quantum-wire arrays using standard procedure [31], [33]. The results of such calculations are shown in Fig. 8. Fig. 8(a) shows the material gain as a function of injected carrier density. Fig. 8(b) shows the modal gain as a function of radiative current density. The optical confinement factor is assumed to be 0.0115, which is a typical value for the 100-Å-thick QWR arrays with equal widths of wire and barrier material in a 2- μm thick separate confinement heterostructure [28], [34]. In the calculations, a Gaussian line shape function [3] with the line broadening of 7 meV was assumed and all nonradiative processes are neglected [26]. The optical polarization is assumed to be parallel to the wire direction. The results indicate that TSL and SSL can give much higher gain compared to a quantum well at the same injection level. The sharply peaked and well-localized DOS profile, large subband spacing, and anisotropic momentum matrix element of the TSL and SSL account for this gain enhancement. Although the transparency current density of TSL and SSL is greater than that of the QW, the gain for TSL and SSL increases so rapidly that the actual threshold current for a practical device with finite loss having TSL or SSL active regions would be smaller than QW structure. Larger resonant frequency is also expected due to the larger differential gain [35]. Therefore, the ideal quantum-wire arrays grown on vicinal substrates with high density of wires like TSL

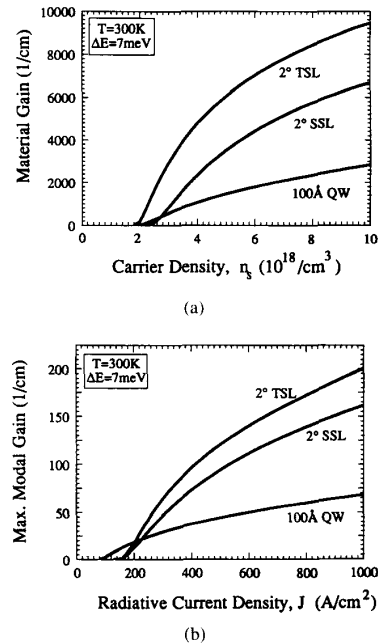


Fig. 8. Comparison of the optical gain of TSL, SSL, and a 100-Å-thick QW. QW and quantum-wire array parameters are the same as the ones described in Fig. 2, 3, and 5. (a) Maximum material gain as a function of carrier density, n_s ($10^{18}/\text{cm}^3$), (b) maximum modal gain as a function of radiative current density, J (A/cm^2). The Gaussian line shape function with 7 meV line broadening has been assumed and nonradiative mechanism have not been included. The optical polarization has been assumed to be parallel to $[1\bar{1}0]$ direction, i.e., to the wire axis.

or SSL can increase the resonant frequency and reduce the threshold current by 2–3 times compared to the conventional QW structure. The effects of imperfections on the optical properties of lateral superlattices can be found elsewhere [27], [36]–[37].

IV. CONCLUSION

In this work, a finite-element method to numerically solve the Luttinger–Kohn Hamiltonian which is commonly used to investigate valence band structure of quantum structures is developed. The required variational functional is formulated through integration by parts with proper boundary conditions. The validity of this functional is verified using Euler equation. The accuracy of the approach is confirmed by comparing its results for energy eigenstates of a quantum well and a quantum wire to other published results. This method offers a significant computational advantage compared to other methods and can be applied to any arbitrarily shaped geometry. Quantitative values for the strength of optical transitions and optical gain of a QW, TSL, and SSL are obtained and compared. The effect of wire-to-wire coupling present in TSL and SSL is also quantitatively investigated. This coupling strongly affects the density of states and optical gain. The resulting optical gain in the ideal tilted superlattice and serpentine superlattice shows 2–3 times enhanced magnitude compared to a conventional quantum-well structure at the same injection level.

$$f_{cn}(E) = \begin{cases} 0 & E < E_n \\ \frac{\sqrt{m_{nx}m_{ny}}}{\pi L_z \hbar^2} & E_n \leq E < E_{nyc} \\ \frac{\sqrt{m_{nx}m_{ny}}}{\pi L_z \hbar^2} \frac{\pi}{2} \left[\sin^{-1} \sqrt{\frac{E_{nyc} - E_n}{E - E_n}} + \sqrt{\frac{m_{nyu}}{m_{ny}}} \log \left(\frac{\sqrt{E - E_{nyc}} - \sqrt{E_{nyu} - E_{nyc}}}{\sqrt{|E - E_{nyu}|}} \right) \right] & E_{nyc} \leq E \end{cases} \quad (\text{A-5})$$

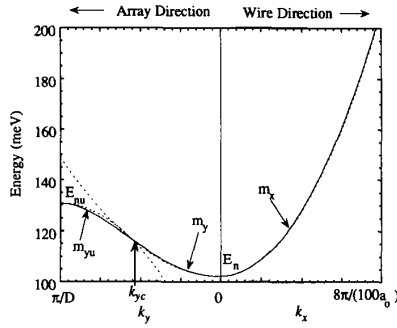


Fig. 9. $E-k$ diagram of a tilted superlattice. Wire material is GaAs and the surrounding material is $\text{Al}_{0.25}\text{Ga}_{0.75}\text{As}$. Wire width and the wire separation are both 40.5 Å, and the wire thickness is 100 Å. The dotted lines are parabolas fitted to the $E-k$ dispersion curve by adjusting the effective masses, m_x , m_y , m_{nyu} , and k_{yc} .

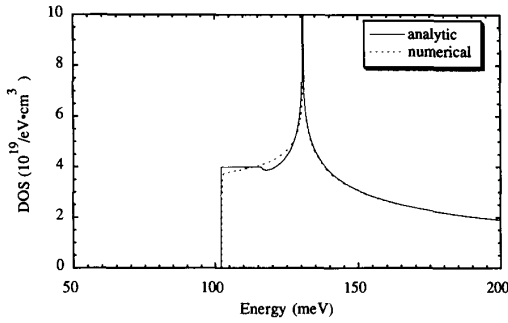


Fig. 10. Density of states function of the TSL shown in Fig. 9. The solid line is calculated from the analytic expressions derived in the Appendix and the dotted line is calculated numerically using the $E-k$ diagram.

APPENDIX

The density of states function of the conduction band in quantum-wire structure can be written [23]

$$f_c(E) = \frac{2}{\pi L_y L_z} \sum_n \int_{-\pi/D}^{\pi/D} \frac{L_y}{2\pi} \sqrt{\frac{m_{nx}}{2\hbar^2}} \frac{H(E - E_n(k_y))}{\sqrt{E - E_n(k_y)}} dk_y \quad (\text{A-1})$$

where $H(x)$ is step function, i.e., $H(x \geq 0) = 1$ and $H(x < 0) = 0$. Here n denotes the n th subband and m_{nx} is the effective mass at the n th subband zone center along the wire direction. Wires are along x -direction and they form an array along y -direction with periodicity D . A typical $E-k$ diagram along the array direction, $E_n(k_y)$, can be approximated as two parabolas. This is illustrated in Fig. 9, where the $E-k$ diagram of a tilted superlattice is plotted. The period D is 81 Å and the wire width and the wire separation are both 40.5 Å. The wire thickness is 100 Å. The wire material is GaAs

and the surrounding material is $\text{Al}_{0.25}\text{Ga}_{0.75}\text{As}$. If one defines effective masses as shown in Fig. 9, the $E-k$ diagram can be expressed as

$$E_{ny}(k_y) = \begin{cases} E_n + \frac{\hbar^2 k_y^2}{2m_{ny}} & \text{for } |k_y| \leq k_{yc} \\ E_{nu} - \frac{\hbar^2 (\frac{\pi}{D} - k_y)^2}{2m_{nyu}} & \text{for } k_{yc} \leq |k_y| \leq \frac{\pi}{D} \end{cases} \quad (\text{A-2})$$

where k_{yc} is the inflection point on the $E-k$ dispersion along k_y , m_{ny} is the effective mass at the n th subband zone center along the array direction, and m_{nyu} is another effective mass at the top of the miniband. E_{nu} is the energy level at the top of the n th miniband. Then the m_{ny} and m_{nyu} can be approximated as

$$\frac{1}{m_{ny}} = \frac{1}{\hbar^2} \left. \frac{\partial^2 E_{ny}(k_y)}{\partial k_y^2} \right|_{k_y=0} \approx \frac{8}{\hbar^2} \frac{(E_{nyc} - E_n)D^2}{\pi^2(1 + \eta)^2} \quad (\text{A-3})$$

$$\frac{1}{m_{nyu}} = \frac{-1}{\hbar^2} \left. \frac{\partial^2 E_{ny}(k_y)}{\partial k_y^2} \right|_{k_y=\pi/D} \approx \frac{8}{\hbar^2} \frac{(E_{nu} - E_{nyc})D^2}{\pi^2(1 - \eta)^2} \quad (\text{A-4})$$

with $E_{nyc} = E_n(k_{yc})$. Here, η is defined as the deviation of the inflection point, k_{yc} , from $\pi/2D$, i.e., $\eta \equiv (k_{yc} - \pi/2D)/(\pi/2D)$.

Now if one inserts (A-2) into (A-1) and performs the integration analytically, the density of states of n th subband in the superlattice quantum wire can be expressed as (A-5) found at the top of the page. Therefore, the conduction band density of states function becomes a step function when $E_n \leq E < E_{nyc}$ with a step height $\sqrt{m_{nx}m_{ny}}/\pi L_z \hbar^2$. In Fig. 10, the density of states functions are plotted using the analytic result given in (A-5) and also using numerical calculations using the $E-k$ diagram. The results obtained numerically and analytically agree quite well.

REFERENCES

- [1] M. Sundaram, S. A. Chalmers, P. E. Hopkins, and A. C. Gossard, "New quantum structures," *Science*, vol. 254, pp. 1326-1335, 1991.
- [2] M. Tuchiya, J. M. Gaines, R. H. Yan, R. J. Simes, P. O. Holtz, L. A. Coldren, and P. M. Petroff, "Optical anisotropy in a quantum-well-wire array with two-dimensional quantum confinement," *Phys. Rev. Lett.*, vol. 62, pp. 466-469, 1989.
- [3] I. Suemune and L. A. Coldren, "Band-mixing effects and excitonic optical properties in GaAs quantum wire structures—comparison with the quantum wells," *IEEE J. Quantum Electron.*, vol. QE-24, pp. 1778-1790, 1988.
- [4] J. M. Gaines, P. M. Petroff, H. Kroemer, R. J. Simes, R. S. Geels, and J. H. English, "MBE growth of tilted GaAs/AlAs superlattices by deposition of fractional on vicinal (001) substrates," *J. Vac. Sci. Technol. B*, vol. 6, pp. 1378-1381, 1988.
- [5] E. Kapon, D. M. Hwang, and R. Bhat, "Stimulated emission in semiconductor quantum wire heterostructures," *Phys. Rev. Lett.*, vol. 63, pp. 430-433, 1989.

- [6] P. M. Petroff, M. S. Miller, Y. T. Lu, S. A. Chalmers, H. Metiu, H. Kroemer, and A. C. Gossard, "MBE growth of tilted superlattices: Advances and novel structures," *J. Crystal Growth*, vol. 111, pp. 360-365, 1991.
- [7] M. Sweeny, J. Xu, and M. Shur, "Hole subbands in one-dimensional quantum well wires," *Superlattices Microstructures*, vol. 4, pp. 623-626, 1988.
- [8] D. J. Searles and E. I. von Nagy-Felsobuki, "Numerical experiments in quantum physics: Finite-element method," *Amer. J. Phys.*, vol. 56, pp. 444-448, 1988.
- [9] K. Kojima, K. Mitsunaga, and K. Kyuma, "Calculation of two-dimensional quantum confined structures using the finite element method," *Appl. Phys. Lett.*, vol. 55, p. 882, 1989.
- [10] C. Pryor, "Electronic structure and optical properties of serpentine superlattice quantum wire arrays," *Phys. Rev. B*, vol. 44, pp. 12912-12917, 1991.
- [11] D. S. Citrin and Y.-C. Chang, "Valence-subband structures of GaAs/Al_xGa_{1-x}As quantum wires: The effect of split-off bands," *Phys. Rev. B*, vol. 40, pp. 5507-5514, 1989.
- [12] T. Yamauchi, T. Takahashi, and Y. Arakawa, "Tight binding analysis for quantum wire lasers and quantum-wire infrared detectors," *IEEE J. Quantum Electron.*, vol. 27, pp. 1817-1823, 1991.
- [13] J. M. Luttinger and W. Kohn, "Motion of electrons and holes in perturbed periodic fields," *Phys. Rev.*, vol. 97, pp. 869-883, 1955.
- [14] D. Marcuse, *Principles of Quantum Electronics*. New York: Academic, 1980.
- [15] S. Corzine, private communication.
- [16] A. T. Meney, "Orientation dependence of subband structures and optical properties in GaAs-AlGaAs quantum wells: [001], [111], [110] and [310] growth directions," *Superlattices Microstructures*, vol. 11, pp. 31-40, 1992.
- [17] M. Altarelli, "Electronic structure and semiconductor-semiconductor transition in InAs-GaSb superlattices," *Phys. Rev. B*, vol. 28, pp. 842-845, 1983.
- [18] K. Nakamura, A. Shimizu, M. Koshiba, and K. Hayata, "Finite-element analysis of quantum wells of arbitrary semiconductors with arbitrary potential profiles," *IEEE J. Quantum Electron.*, vol. QE-25, pp. 889-895, 1989.
- [19] K.-J. Bathe and E. L. Wilson, *Numerical Methods in Finite Element Analysis*. Englewood Cliffs, NJ: Prentice-Hall, 1976.
- [20] P. P. Silvester and R. L. Ferrari, *Finite Elements for Electrical Engineers*. London: Cambridge University Press, 1983.
- [21] K. Nakamura, A. Shimizu, M. Koshiba, and K. Hayata, "Finite-element analysis of the miniband structures of semiconductor superlattices with arbitrary periodic potential profiles," *IEEE J. Quantum Electron.*, vol. 27, pp. 2035-2041, 1991.
- [22] R. C. Miller, D. A. Kleinman, and A. C. Gossard, "Energy-gap discontinuities and effective masses for GaAs-Al_xGa_{1-x}As quantum wells," *Phys. Rev. B*, vol. 29, pp. 7085-7087, 1984.
- [23] Y. Arakawa and H. Sakaki, "Multidimensional quantum well laser and temperature dependence of its threshold current," *Appl. Phys. Lett.*, vol. 40, pp. 939-941, 1982.
- [24] G. Bastard and J. A. Brum, "Electronic states in semiconductor heterostructures," *IEEE J. Quantum Electron.*, vol. QE-22, pp. 1625-1644, 1986.
- [25] D. Ahn and S.-L. Chuang, "Optical gain and gain suppression of quantum well lasers with valence band mixing," *IEEE J. Quantum Electron.*, vol. 26, pp. 13-24, 1990.
- [26] S. W. Corzine, R. H. Yan, and L. A. Coldren, "Strained InGaAs/AlGaAs quantum wells including valence-band mixing effects," *Appl. Phys. Lett.*, vol. 57, pp. 2835-2837, 1990.
- [27] J. C. Yi and N. Dagli, "Density of states enhancement in GaAs-AlGaAs quantum wire arrays," unpublished.
- [28] J. C. Yi, N. Dagli, and L. A. Coldren, "Investigation of tilted superlattices for quantum wire laser applications," *Appl. Phys. Lett.*, vol. 59, pp. 3015-3017, 1991.
- [29] P. C. Sercel and K. J. Vahala, "Polarization dependence of optical absorption and emission in quantum wires," *Phys. Rev. B*, vol. 44, pp. 5681-5691, 1991.
- [30] C. R. McIntyre and L. J. Sham, "Theory of luminescence polarization anisotropy in quantum wires," *Phys. Rev. B*, vol. 45, pp. 9443-9446, 1992.
- [31] K. Y. Cheng, E. M. Stellini, P. J. Pearah, A. C. Chen, A. M. Moy, and K. C. Hsieh, "Fabrication and characterization of AlGaInP multiple-quantum-wire lasers," in *Proc. Int. Electron Dev. Meet.*, '92, pp. 875-878.
- [32] J. C. Yi, H. Weman, M. S. Miller, N. Dagli, P. M. Petroff, and J. L. Merz, "Photoluminescence lifetime of serpentine superlattice quantum wire arrays," in *Proc. Int. Quantum Electron. Conf.*, Vienna, 1992, paper PTh057.
- [33] R. Nagarajan, T. Kamiya, and A. Kurobe, "Band filling in GaAs/AlGaAs multi-quantum well lasers and its effect on the threshold current," *IEEE J. Quantum Electron.*, vol. QE-25, pp. 1161-1170, 1989.
- [34] G. P. Agrawal and N. K. Dutta, *Long Wavelength Semiconductor Lasers*. New York: Van Nostrand Reinhold, 1986.
- [35] Y. Arakawa, K. Vahala, A. Yariv, and K. Lau, "Enhanced modulation bandwidth of GaAlAs double heterostructure lasers in high magnetic fields: Dynamic response with quantum wire effects," *Appl. Phys. Lett.*, vol. 47, pp. 1142-1144, 1985.
- [36] J. C. Yi and N. Dagli, "Optical properties of serpentine superlattices on GaAs vicinal substrates for quantum wire laser applications," *Appl. Phys. Lett.*, vol. 61, pp. 219-221, 1992.
- [37] A. K. Myers-Beaghton, J. P. G. Taylor, D. D. Vvedensky, K. J. Huggill, and A. MacKinnon, "Growth kinetics and electronic characteristics of quantum wires," *J. Crystal Growth*, vol. 111, pp. 328-332, 1991.
- [38] D. E. Aspens, S. M. Kelso, R. A. Rogan, and R. Bhat, "Optical properties of Al_xGa_{1-x}As," *J. Appl. Phys.*, vol. 60, pp. 754-767, 1986.
- [39] X. Landolt-Bornstein, in *Numerical Data and Functional Relationship in Science and Technology*, O. Madelung, Ed. Berlin: Springer, 1982, New Series III, vols. 17 and 22.



Jong Chang Yi was born in Taegoo, South Korea, on December 20, 1960. He received the B.S.E. degree from Seoul National University, and the M.S. degree from Korea Advanced Institute of Science and Technology in 1983 and 1985, respectively, and the Ph.D. degree in electrical engineering from the University of California, Santa Barbara, for work on nanostructure quantum-wire lasers and electron waveguides, during 1989-1994.

During 1985-1989, he worked as a researcher at the Applied Optics Laboratory in Korea Institute of Science and Technology, Seoul, Korea, on high-speed integrated optic modulators. He is currently an Assistant Professor in the Electrical Engineering Department, Hong Ik University, Seoul, Korea. His research interests include high-speed optoelectronic TDM devices and exotic nanostructures for quantum optoelectronic phenomena.



Nadir Dagli (S'77-M'86) was born in Ankara, Turkey. He received the B.S. and M.S. degrees in electrical engineering from Middle East Technical University, Ankara, Turkey, in 1976 and 1979, respectively, and the Ph.D. degree in electrical engineering from the Massachusetts Institute of Technology, Cambridge, MA, in 1986. During his Ph.D. research, he worked on the design, fabrication, and modeling of guided-wave integrated optical components in III-V compound semiconductors.

He also worked on III-V materials preparation by LPE and the modeling and analysis of heterojunction bipolar transistor for microwave and millimeter-wave applications.

After graduation, he joined the Electrical and Computer Engineering Department at the University of California, Santa Barbara, where he is currently an Associate Professor. His current interests are design, fabrication, and modeling of guided-wave components for optical integrated circuits, solid-state microwave and millimeter-wave devices, calculations on the optical properties of quantum wires, electron waveguides, and novel quantum interference devices based on electron waveguides.

Dr. Dagli was awarded NATO science and IBM prodoctoral fellowships during his graduate studies. He is the recipient of the 1990 UCSB Alumni Distinguished Teaching Award and the 1990 UC Regents Faculty Fellowship.